



LiCoMnO₄@Graphite: A 5.2 V hybrid cathode for simultaneous anion and cation intercalation/de-intercalation

Sreekumar Sreedeeep^a, Karayi Mangat Athira^a, Yun-Sung Lee^{b,*}, Vanchiappan Aravindan^{a,**}

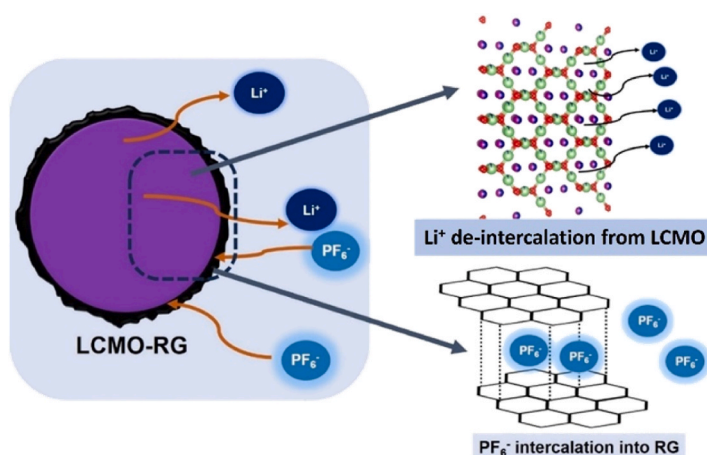
^a Department of Chemistry, Indian Institute of Science Education and Research (IISER), Tirupati-517619, Andhra Pradesh, India

^b School of Chemical Engineering, Chonnam National University, Gwang-ju, 61186, Republic of Korea

HIGHLIGHTS

- Simultaneous insertion/extraction of anion and cation is realized in LiCoMnO₄@Graphite.
- Various electrolyte solutions are studied and optimized.
- Full-cell is fabricated with LTO anode, Li-metal and anode-less configuration is explored.
- LiCoMnO₄@Graphite/LTO cells are studied from −10 to 70 °C to validate the feasibility.

GRAPHICAL ABSTRACT



ARTICLE INFO

Keywords:

High voltage cathode
Anion intercalation
Li-extraction
Dual-ion
Anode less

ABSTRACT

Here, we report the simultaneous dual-ion (both Li⁺ and PF₆⁻) intercalation/de-intercalation in a hybrid high-voltage LiCoMnO₄@Graphite (LCMO_RG) cathode. Compared to the pristine LCMO, the feasible intercalation of PF₆⁻ into RG in LCMO_RG will further enhance their energy density. Also, the galvanostatic cycling profile of LCMO_RG exhibits excellent cycle stability and electrochemical performance compared to pristine LCMO with different electrolyte solutions. The diffusion coefficient has been evaluated from the electrochemical impedance spectroscopy plot, which exhibits a magnitude in the order of $\sim 10^{-14}$ m² s⁻¹. A post-analysis of the cycled LCMO_RG electrodes was performed using XRD and XPS analysis to comprehend any phase change or structural distortion accompanying electrochemical cycling. Full-cell studies have been performed for the LCMO_RG against Li₄Ti₅O₁₂ (LTO) as an anode, using the optimized electrolyte combination. Further, an anode-less configuration was also performed against Cu-strip as a counter electrode to validate the potential use of the hybrid cathode.

* Corresponding author.

** Corresponding author.

E-mail addresses: leey@chonnam.ac.kr (Y.-S. Lee), Aravind.van@gmail.com (V. Aravindan).

<https://doi.org/10.1016/j.jpowsour.2025.238366>

Received 22 February 2025; Received in revised form 2 September 2025; Accepted 8 September 2025

Available online 15 September 2025

0378-7753/© 2025 Elsevier B.V. All rights are reserved, including those for text and data mining, AI training, and similar technologies.

1. Introduction

Energy storage technologies have advanced significantly since the advent of Lithium-ion battery (LIBs) technologies. The desirable features, such as high energy and power density, low reduction potential (-3.04 V vs. Li), and low memory effect, have led to the wide-scale applicability of LIBs in laptops, mobile phones, and emission-free electric vehicles (EVs) [1–4]. As the demand for EVs is growing day by day, a parallel growth in research and development is occurring among the LIBs. Prominent research in LIBs is concentrated on enhancing their energy density [38]. As energy density is proportional to the specific capacity and operating potential, there is a huge necessity for the development of materials with high specific capacity and operating potential. Although specific capacity is inherent to a material, modifying the working potential is a better strategy to enhance the energy density. As the cathode contributes a substantial share of energy density in a LIB due to its high operating potential, it necessitates the development of various cathode materials. Conventional cathodes, such as layered LiCoO_2 , possess severe safety issues due to O_2 release at a high state of charge. Although the commercialization of olivine-phased LiFePO_4 has been achieved, the low working potential of the $\text{Fe}^{3+/2+}$ redox couple (~ 3.4 V vs. Li) restricts its usage towards high-voltage applications [5–9]. But the commercialization of spinel-phased $\text{LiNi}_{0.5}\text{Mn}_{1.5}\text{O}_4$ (LNMO) has paved the way for the development of other high-voltage cathodes, such as spinel-phased LiCoMnO_4 and olivine-phased LiCoPO_4 [10–26]. Hence, sufficient efforts have to be devoted to developing these high-voltage cathodes to power up the development of the next-generation EVs.

Dual-ion batteries (DIBs) are a new class of energy storage systems. The fast-charging capability, low material cost, and ease of recyclability make DIBs the next-generation battery technology [21–26]. Unlike conventional LIBs, the charge storage mechanism differs in the case of DIBs. In a DIB, the electrolyte is the active component supplying the ions (cations and anions) during the charge-discharge. On charging, the anions (PF_6^- , BF_4^- , etc.) and cations (Li^+ , Na^+ , etc.) from the electrolyte will intercalate into the cathode and anode, respectively, while the ions are released back into the electrolyte during discharge. Graphite, owing to its redox amphoteric behavior, has been used both as an anode and cathode for DIBs, as it can form graphite-intercalation compounds (GICs) with both anions (e.g. $\text{C}_{24}\text{PF}_6^-$) and cations (e.g. LiC_6). The ease of availability, low cost, and eco-friendly nature of graphite have led to extensive research in the field of graphite-based DIBs [35–37]. Furthermore, graphite's high anion intercalation potential (~ 5.2 V vs. Li) enhances the energy density, making it favorable for use in various high-energy and power applications [27].

The state-of-the-art research in DIBs is focused on (i) the development of host materials with excellent ion storage ability and (ii) electrolyte modification to achieve high-voltage stability. Despite graphite being considered an excellent ion-storage host for DIBs, its usage is subject to various setbacks, including low cycle stability due to exfoliation/flaking, low specific capacity (~ 62 mAh g^{-1} for $\text{C}_{24}\text{PF}_6^-$), and surface catalytic reaction leading to parasitic side-reactions with the electrolyte. Therefore, the idea of hybrid cathode materials emerged out of the need for a suitable host material. The hybrid cathodes integrate the specific advantages of two ion-storage host materials—typically a LIB cathode and a DIB cathode, particularly graphite. The underlying charge storage mechanism in a hybrid cathode occurs through a path by which, during charging, anions from the electrolyte intercalate into the anion storage host of the hybrid cathode with a simultaneous de-intercalation of Li-ions from the LIB cathode. On the other hand, the discharging occurs with the intercalation of Li-ions into the LIB cathode and simultaneous de-intercalation of anions into the electrolyte. Winter *et al.* [27] reported $\text{LiNi}_{0.5}\text{Mn}_{1.5}\text{O}_4$ /graphite hybrid cathode cycled in concentrated electrolytes, which exhibits excellent cycle stability and coulombic efficiency compared to pristine $\text{LiNi}_{0.5}\text{Mn}_{1.5}\text{O}_4$ due to the simultaneous anion and cation intercalation in the former compared to the latter, but

limited to the cut-off potential of 5 V (vs. Li). This eventually hinders the formation of the complete graphite intercalation compound. In addition, other hybrid cathodes, such as LiFePO_4 /graphite, $\text{LiFe}_{0.6}\text{Mn}_{0.4}\text{PO}_4$ /graphite flake, etc., have been reported in recent years [28–30]. However, a major setback with all the aforementioned hybrid cathodes is their low operating window; the graphite serves only as a conductive additive or partial anion intercalation for the case of $\text{LiNi}_{0.5}\text{Mn}_{1.5}\text{O}_4$ /graphite rather than the formation of the binary graphite intercalation compound (e.g., $\text{C}_{24}\text{PF}_6^-$), which occurs at a high potential >5 V (vs. Li). In addition, the large volume expansion due to graphite exfoliation is still persistent among these cathodes.

Taking into account various aspects of the DIBs and the hybrid cathodes, here we report a hybrid high-voltage cathode by combining a spinel-phased LiCoMnO_4 (LCMO) with recovered graphite (RG) from spent LIBs using a reported procedure, denoted as LCMO_RG [31]. Conceptually, the dual intercalation of anion and cation will enhance the power capability of the system compared to the conventional cation-based system. Also, the high anion intercalation potential will further contribute to the enhanced energy density. The LCMO_RG composites have been prepared by dry-mixing the co-precipitation-synthesized LCMO with RG, varying the RG amount from 5 to 40%. The high operating potential of LCMO_RG promotes facile anion intercalation into RG compared to the aforementioned hybrid cathodes. Also, the expanded large interlayer spacing of RG (~ 0.35 Å) compared to commercial graphite (~ 0.335 Å) enables the favorable intercalation of bulky anions such as PF_6^- . The electrolyte modification using linear carbonates, such as dimethyl carbonate (DMC) and ethyl methyl carbonate (EMC) with fluoroethylene carbonate (FEC) as an additive, has been carried out to eliminate the usage of ethylene carbonate (EC). The FEC forms a thinner, more stable SEI layer, facilitating the anion (PF_6^-) intercalation into RG. In contrast, EC forms a thicker SEI layer that hinders the anion intercalation into RG. Further, FEC forms a LiF-rich SEI layer that enhances the cycle stability of LCMO_RG even at high operating potential. The full-cell fabrication has been carried out against $\text{Li}_4\text{Ti}_5\text{O}_{12}$ (LTO) as an anode to illustrate its practical applicability. In addition, an anode-less cell configuration has been performed by coupling the optimized LCMO_RG with Cu as a counter electrode.

2. Experimental section

2.1. Synthesis of LCMO and preparation of LCMO_RG

The synthesis of the LCMO was carried out using a co-precipitation method. The precursor solution was prepared by dissolving stoichiometric amounts of the precursors, including Co ($(\text{CH}_3\text{COO})_2 \cdot 6\text{H}_2\text{O}$ (Sigma-Aldrich, $\geq 98\%$) and Mn ($(\text{CH}_3\text{COO})_2 \cdot 7\text{H}_2\text{O}$ (Sigma-Aldrich, $\geq 99\%$), in deionized water, followed by the addition of 30 ml of ethanol. The precipitation of the precursor solution was initiated with the addition of a stoichiometric amount of $(\text{NH}_4)_2\text{CO}_3$ (Sigma-Aldrich, $\geq 99.99\%$) dissolved in deionized water. The precipitate was allowed to settle down, washed with deionized water and ethanol, and dried overnight. The dried sample was calcined to a temperature of 400°C for 2 h. The as-obtained sample was then dispersed in an ethanol solution containing a stoichiometric amount of CH_3COOLi dissolved in it for the Li-source. A slow drying process evaporated out the ethanol, and the sample was then calcined to a temperature of 800°C for 12 h.

The LCMO_RG hybrid cathode was prepared by mixing the LCMO along with RG using a mortar and pestle at specific weight ratios of 95–5, 90–10, 80–20, and 60–40.

2.2. Electrolyte preparation

This investigation utilized two distinct electrolyte combinations: (i) 1M LiPF_6 dissolved in DMC (Sigma-Aldrich), (ii) 1M LiPF_6 dissolved in EMC (Sigma-Aldrich), in both cases 5 wt% (by volume) of FEC (TCI,

≥98%) was added as an electrolyte additive.

2.3. Electrochemical characterization and cell fabrication

The electrodes are prepared either by a slurry-casting method or by preparing a free-standing film. The LCMO_RG electrodes are prepared by mixing the active material with conductive carbon (Acetylene black, Alfa-easier) and binder (TAB-2, Teflonized acetylene black) in a weight ratio of 10:2:2 (in mg) using a mortar and pestle with ethanol as a medium. A free-standing film was obtained at the end of the mixing, which was then cast on a stainless-steel mesh (Goodfellow, 14 mm) using a pellet maker and a hydraulic press. The electrode was kept overnight to remove the moisture content. The cell fabrication was carried out with a CR2016 coin-cell set-up with glass microfibre (Whatman, 1825-047, UK) using 100 μ l of either DMC_FEC or EMC_FEC electrolyte combination in an Ar-filled glovebox (MBraun, Germany) with <0.1 ppm for both H₂O and O₂ levels. The preliminary half-cell studies were conducted to optimize the suitable LCMO_RG within a potential range of 3–5.2 V vs. Li.

For the full-cell fabrication, the optimized LCMO_RG was paired against Li₄Ti₅O₁₂ (LTO) as an anode. Also, an anode-less configuration was carried out with a Cu-strip as a counter electrode. The LTO electrode was fabricated by a slurry coating method, in which a homogenous slurry was prepared by the mixing of the active material, conductive carbon (Acetylene black, Alfa-easier), and binder (TAB, Teflonized acetylene black) in a weight ratio of 80:10:10 with N-methyl-2-pyrrolidone (NMP) as the solvent. The as-obtained slurry was then coated on an Al-foil using a doctor-blade set-up and then kept for drying. The electrodes were then cut from the foil with a 14 mm diameter using an electrode cutter. The electrodes were kept for drying before inserting them into the glovebox, followed by full-cell fabrication by pairing LCMO_RG against LTO in an Ar-filled glovebox using 100 μ l of the optimized electrolyte combination. The ratio of loading of LTO to LCMO_RG, that is the N/P ratio, comes to be 1.04. The fabricated full-cell was tested within a 1.5–3.7 V potential range in a battery tester (Biologic, France). Also, temperature studies for the full cells were conducted in an environmental chamber (Espec, Japan) within a range of –10 to 60 °C.

Apart from the full- and half-cells, a symmetric cell has been fabricated with configurations of SS/electrolyte-soaked separator/SS (SS-stainless steel) for the calculation of ionic conductivity and Li/electrolyte-soaked separator/Li for the transference number calculation and to determine the stability of electrolyte. Also, asymmetric cells were fabricated with configuration, SS/electrolyte-soaked separator/Li for the linear-sweep voltammetry (LSV), and Li/electrolyte-soaked separator/Cu for determining the electrolyte stability. In addition, the anode-less cell was fabricated by pairing the LCMO_RG with a Cu strip using the optimized electrolyte combination and tested within the potential window of 2.9–5.1 V in a battery tester.

2.4. Material characterization

The structural and phase characteristics of the LCMO_RG composites were elucidated from the X-ray diffraction (XRD, Rigaku, Smart lab 9 kW, monochromatic Cu K α radiation (λ = 1.5406 Å) analysis performed within the 2 θ range of 10–90° at a scan-rate of 0.1° min^{–1}. Raman spectroscopy (LabRam HR800 UV Raman microscope, Horiba Jobin-Yvon, France) analysis was carried out to understand the nature of RG in the LCMO_RG composite. In addition, the surface elemental analysis was carried out by X-ray photoelectron spectroscopy (XPS, with a multilab instrument with a monochromatic Al K α radiation $h\nu$ = 1486.6 eV) analysis. The shape and morphology of the LCMO_RG were further analyzed using FE-SEM (ZEISS) and TEM (TECNAL, Philips, the Netherlands, 200 keV) analysis. In addition, the EDS analysis was performed to examine the homogeneity in the elemental distribution of the sample.

2.5. Theoretical calculation

Density functional theory (DFT) calculations were carried out using a B3LYP function and a 6-31G basis set. The HOMO-LUMO energy gap for the different electrolyte components has been calculated to understand the overall stability of the electrolyte. In addition, interaction studies were performed with the electrolyte additive and solvent with the Li⁺ and PF₆[–] ions in the electrolyte.

3. Result and discussion

3.1. Material characterizations

The XRD analysis (Fig. 1a, S14) has been carried out to reveal the phase and structural aspects of LCMO_RG. The diffraction peaks at 2 θ values of 19°, 37°, 44°, and 65° indicate the (111), (311), (444), and (440) crystal planes of LCMO, while the peak at 2 θ value of 26° corresponds to the (002) crystal plane of the 2H phase (ABA ...) of the RG component. In addition, the XRD analysis of RG (Fig. S1) exhibits a highly intense peak corresponding to the (002) plane at a 2 θ value of 26°, which is in agreement with the diffraction peak present in LCMO_RG. In addition, the interlayer spacing of the RG component has been calculated from Bragg's equation to be ~3.42 Å, which is much higher compared to the commercial graphite (~3.335 Å), thereby reducing the occurrence of volume expansion due to bulky anion intercalation [31]. Also, a proportional rise in the intensity of the diffraction peak can be observed for the (002) plane as the RG component is increased from 5 to 40 wt%. Raman spectral analysis (Fig. 1b) of LCMO_RG indicates a less intense D-band (~1346 cm^{–1}) and an intense G-band (~1580 cm^{–1}), which illustrates the RG component. Also, a peak at 2708 cm^{–1} for the LCMO_RG indicates the 2-D peak in the RG. The ratio between the intensity of the D to the G-band (I_D/I_G ~0.67) depicts an ordered arrangement in the RG along with a low defect concentration ($I_D/I_D + I_G$ = 0.35). The XPS analysis has been carried out to investigate the surface elemental composition of LCMO_RG. The survey spectrum (Fig. 1c) illustrates the presence of Li, C, O, Mn, and Co in the compound (Fig. 1d–g) with a chemical state of Li 1s, C 1s, O 1s, Mn 2p, and Co 2p. The deconvolution of the C 1s core level exhibits peaks corresponding to C–C (284.48 eV), C=C (285.2 eV), and C–O (286.4 eV) modes, which are associated with the RG component in the LCMO_RG hybrid. Meanwhile, the deconvolution of the O 1s core level shows peaks corresponding to metal oxide M (Mn, Co)—O, C=O, and C–O at binding energy values of 529.8, 531.3, and 532.6 eV, respectively. The deconvolution of the Mn 2p core level exhibits two pairs of peaks corresponding to Mn 2p_{1/2} and Mn 2p_{3/2}, while the Co 2p exhibits peaks corresponding to Co 2p_{1/2} and Co 2p_{3/2}. Also, the oxidation state of Co and Mn was evaluated as +3 and +4, respectively. The BET plot (Fig. 1h) of LCMO_RG: 60-40 shows a surface area of ~6.936 m² g^{–1}, while RG exhibits a surface area of 13.4 m² g^{–1}.

Imaging techniques such as FE-SEM (Fig. 2a–c) and TEM (Fig. 2d–g) have been further utilized to understand the shape and morphology of the as-synthesized LCMO_RG:60.40. The FE-SEM images of the LCMO_RG cathode show spherical-shaped LCMO single-crystalline particles covered with flaky RG particles. Further, the individual FE-SEM images of the LCMO and RG are shown in Fig. S2a–f. The TEM images (Fig. 2d–f) depict the RG coating on the surface of LCMO. Also, the SAED pattern clearly illustrates the crystalline nature of the sample. In addition, the EDS mapping (Fig. 2h–l) shows the elemental distribution of C, O, Mn, and Co throughout the compound.

3.2. Theoretical studies

A comparison of the energy gap between the highest occupied molecular orbital (HOMO) and the lowest unoccupied molecular orbital (LUMO) has been illustrated in Fig. S3. The electrolyte stability window can be evaluated from the magnitude of ΔE , $\Delta E = E_{\text{HOMO}} - E_{\text{LUMO}}$, of the

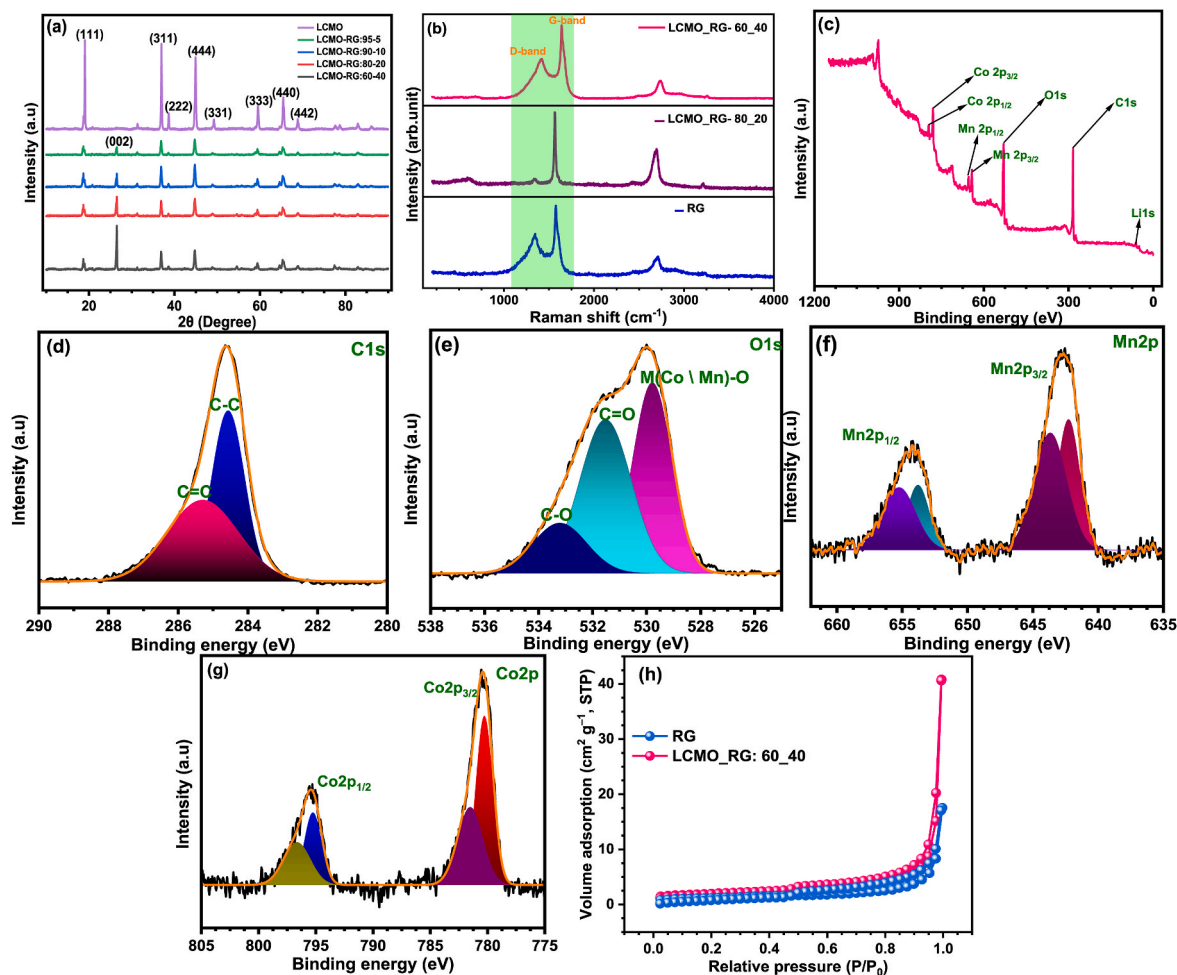


Fig. 1. Structural analysis using (a) XRD, (b) Raman, (c–g) XPS survey spectrum followed by deconvoluted spectra of C 1s, O 1s, Mn 2p, and Co 2p, and (h) N_2 adsorption/desorption isotherms of RG and LCMO_RG:60_40.

different electrolyte combinations. The as-determined magnitude of ΔE is -7.35 , -7.21 , and -8.12 eV, respectively, for DMC, EMC, and FEC. The high electrolyte stability window of DMC ensures better electrolyte stability compared to the EMC. The same has been revealed from the GCD studies wherein the DMC_FEC electrolyte combination exhibits excellent electrolyte stability compared to EMC_FEC. Also, the charge distribution of the different electrolyte components was determined using electrostatic potential (ESP) mapping. Fig. S4 shows the ESP mapping of the different electrolyte components. The ESP mapping exhibits an even charge distribution among the FEC, while the charge distribution among the DMC and EMC is concentrated in a certain portion.

3.3. Electrochemical characterization of the electrolyte

Optimization of the appropriate electrolyte combination has been dealt with in the initial part of the study. The symmetric cell study has been carried out with the cell configuration of $Li \backslash DMC_FEC$ or $EMC_FEC \backslash Li$ at an areal current density of 0.5 mA h cm^{-2} . The symmetric cell (Fig. 3a) $Li \backslash DMC_FEC \backslash Li$ exhibits stable cycling to a duration of ~ 300 h without any initial polarization. In contrast, $Li \backslash EMC_FEC \backslash Li$ exhibits polarization in the initial cycles, and the same persists as the cycling progresses, leading to a decrement in the cycle stability. The enhancement in the cycle stability for the DMC_FEC can be attributed to the high oxidation stability of the DMC. On the other hand, in EMC_FEC, EMC's relatively low oxidation stability compared to DMC further deteriorates its cycle stability and causes high polarization as the cycling progresses.

To further prove this aspect, the linear sweep voltammetry (LSV) (Fig. 3c) of both electrolyte combinations has been carried out in an asymmetric cell configuration of $SS \backslash DMC_FEC$ or $EMC_FEC \backslash Li$. The LSV plot exhibits excellent oxidation stability among the DMC_FEC with an oxidation stability of ~ 4.87 V vs. Li, while the EMC_FEC shows an oxidation stability of ~ 4.3 V vs. Li, hence validating this aspect. The asymmetric cell configuration (Fig. 3b), $Li \backslash DMC_FEC$ or $EMC_FEC \backslash Cu$, has been further studied to understand the stability of both electrolytes towards anode-less cell configuration. Similar to the symmetric cell configuration, the DMC_FEC exhibits superior stability to a duration of ~ 100 h, while the EMC_FEC shows polarization in the initial cycles and remains stable only to a duration of ~ 35 h. The Li-ion transfer kinetics in both the electrolyte combinations have been determined from the activation energy (E_a) (Fig. 3d) using a symmetric cell configuration of $SS \backslash DMC_FEC$ or $EMC_FEC \backslash SS$. The E_a has been evaluated from the magnitude of solution-resistance (R_s) of the Nyquist plot carried out within a temperature range of -10 to 70°C , using the equation given by Refs. [10,11],

$$\ln(\sigma) = \ln(\sigma_0) - \frac{E_a}{R \times T} \quad (i)$$

Where σ is the ionic conductivity, σ_0 is the pre-exponential factor, E_a is the activation energy, T is the respective temperature at which impedance is determined, and R is the universal gas constant ($8.31 \text{ J K}^{-1} \text{ mol}^{-1}$). The magnitude of E_a has been evaluated to be 0.27 and 0.14 eV for EMC_FEC and DMC_FEC, respectively. The as-determined magnitudes of E_a show that the Li-ion kinetics in EMC_FEC are impeded due to

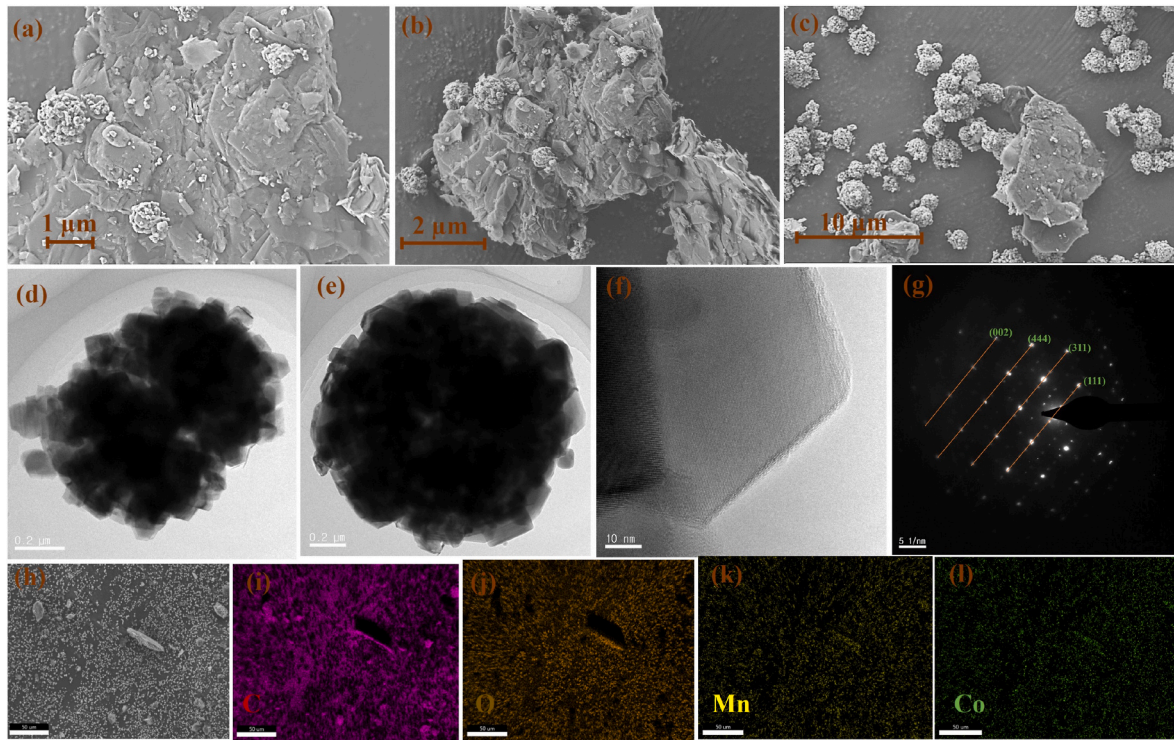


Fig. 2. (a–c) FE-SEM images of LCMO_RG:60–40, (d–g) TEM images of LCMO_RG:60–40, and (h–l) EDS elemental analysis showing the homogenous distribution of elements such as C, O, Mn, and Co in LCMO_RG:60–40.

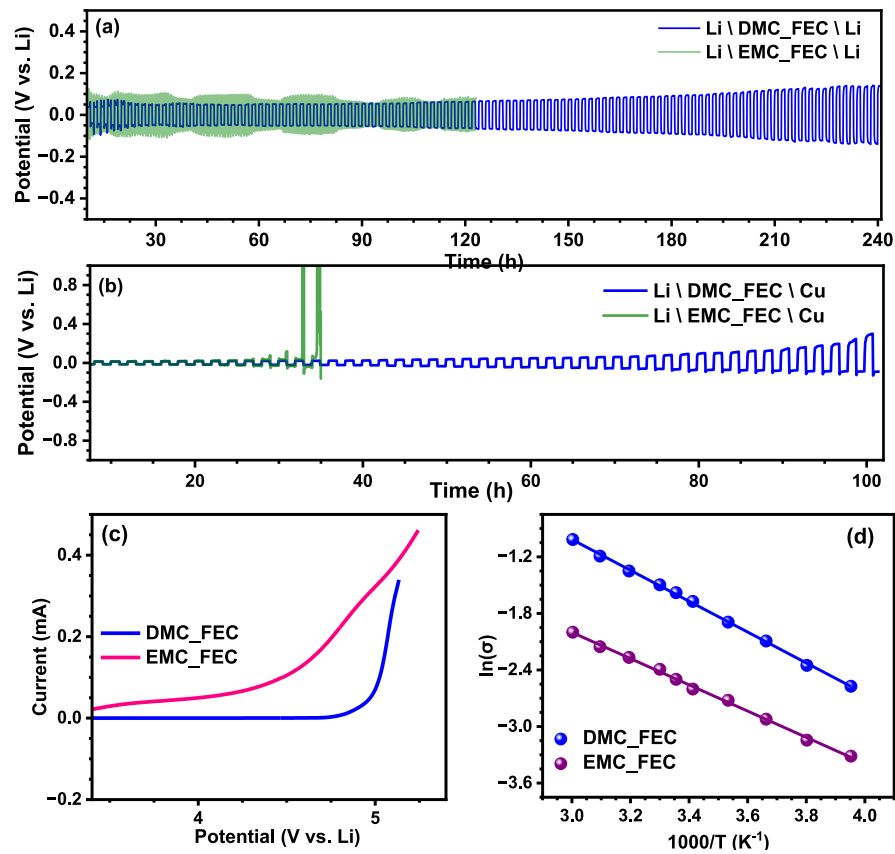


Fig. 3. Plot showing (a) symmetric cell study (Li\\Li), (b) asymmetric cell study (Li\\Cu) carried out at a current density of 50 mA cm⁻², (c) LSV, and (d) Arrhenius plot of the EMC_FEC and DMC_FEC electrolyte combinations.

the large energy barrier, while facile Li-ion kinetics can be observed due to the relatively low energy barrier in DMC_FEC. Therefore, these results are consistent with the fact that the DMC_FEC electrolyte combination outperforms EMC_FEC.

3.4. Half-cell electrochemical study

The galvanostatic charge-discharge (GCD) study has been carried out with LCMO_RG composites with RG ranging from 5 to 40 wt% and tested within a potential window of 3–5.2 V (vs. Li) using electrolyte combinations of DMC_FEC and EMC_FEC. The GCD profile (Fig. 4a–d) of pristine LCMO and LCMO_RG cycled in DMC_FEC exhibits discharge capacities of 82, 104, 106, 107, and 109 mAh g⁻¹ with capacity retentions of 68, 65, 70, 73, 80, and 76% after 100 cycles for 95.5, 90.10, 80.20 and 60.40 composites, respectively. On the other hand, the pristine LCMO and LCMO_RG in the EMC_FEC show a decrement in the electrochemical performance with discharge capacities of 80, 99, 102, 107, and 106 mAh g⁻¹ and capacity retention of 64, 60, 65, 68, and 71% after 100 cycles for 95.5, 90.10, 80.20 and 60.40 composites, respectively. This enhancement in the electrochemical performance, particularly discharge capacity, among the LCMO_RG is attributed to the simultaneous (de-)intercalation of the Li⁺ and PF₆⁻ into LCMO and RG during charge-discharge. This can be observed from the GCD curves wherein the peak at 5.1 V (vs. Li) corresponds to the PF₆⁻ intercalation into RG during charging, while the peak at 4.8 V vs. Li corresponds to the Li⁺ intercalation into LCMO during discharging. In contrast, the absence of this mechanism results in a deterioration in the discharge capacity of the pristine LCMO. Also, the presence of RG on the surface of LCMO in LCMO_RG prevents contact with the electrolyte, thereby mitigating

parasitic side reactions with the electrolyte, which further enhances the cycle stability compared to pristine LCMO.

The dual-ion (de-)intercalation into LCMO_RG has been confirmed from the differential capacity plot (Fig. S5), wherein the peak corresponding to 5.1 V (vs. Li) shows the PF₆⁻ intercalation into the RG while the remaining redox peaks are in agreement with the Li-ion de-/intercalation into the LCMO, hence showing its hybrid nature. In addition, the peak at 5.1 V vs. Li becomes more pronounced as the RG content increases from 20 to 60 wt% due to the increase in the PF₆⁻ intercalation into RG. Based on the preliminary GCD study, the LCMO_RG: 80_20 has been optimized to exhibit superior electrochemical performance. Also, the rate performance study (Fig. 4e) further shows superior electrochemical stability and discharge capacity among the LCMO_RG: 80_20, even at high current densities of 80 and 100 mA g⁻¹, compared to other composites. The suitable electrolyte combination among the DMC_FEC and EMC_FEC has been further confirmed from the rate performance study of LCMO_RG: 80_20 in both these electrolytes, wherein that cycled in DMC_FEC shows superior electrochemical performance with capacity retention of 77% after 50 cycles, while LCMO_RG: 80_20 cycled in EMC_FEC shows poor capacity retention of 66% after 50 cycles. Hence, the suitable electrolyte combination has been optimized to be DMC_FEC. Also, the GCD curves (Fig. S6a–b) for the RG exhibit an initial discharge capacity of 76 mAh g⁻¹ with a capacity retention of 85% after 100 cycles.

The cyclic voltammetry (CV) analysis (Fig. S7a) for the LCMO_RG composites has been conducted at scan rates of 0.1–1 mV s⁻¹ within the potential window of 3.5–5.2 V vs. Li in the electrolyte combinations of DMC_FEC and EMC_FEC. The CV profile of LCMO_RG exhibits a pair of oxidation (3.7 and 4.8 V vs. Li) and reduction (4.7 and 3.4 V vs. Li) peaks

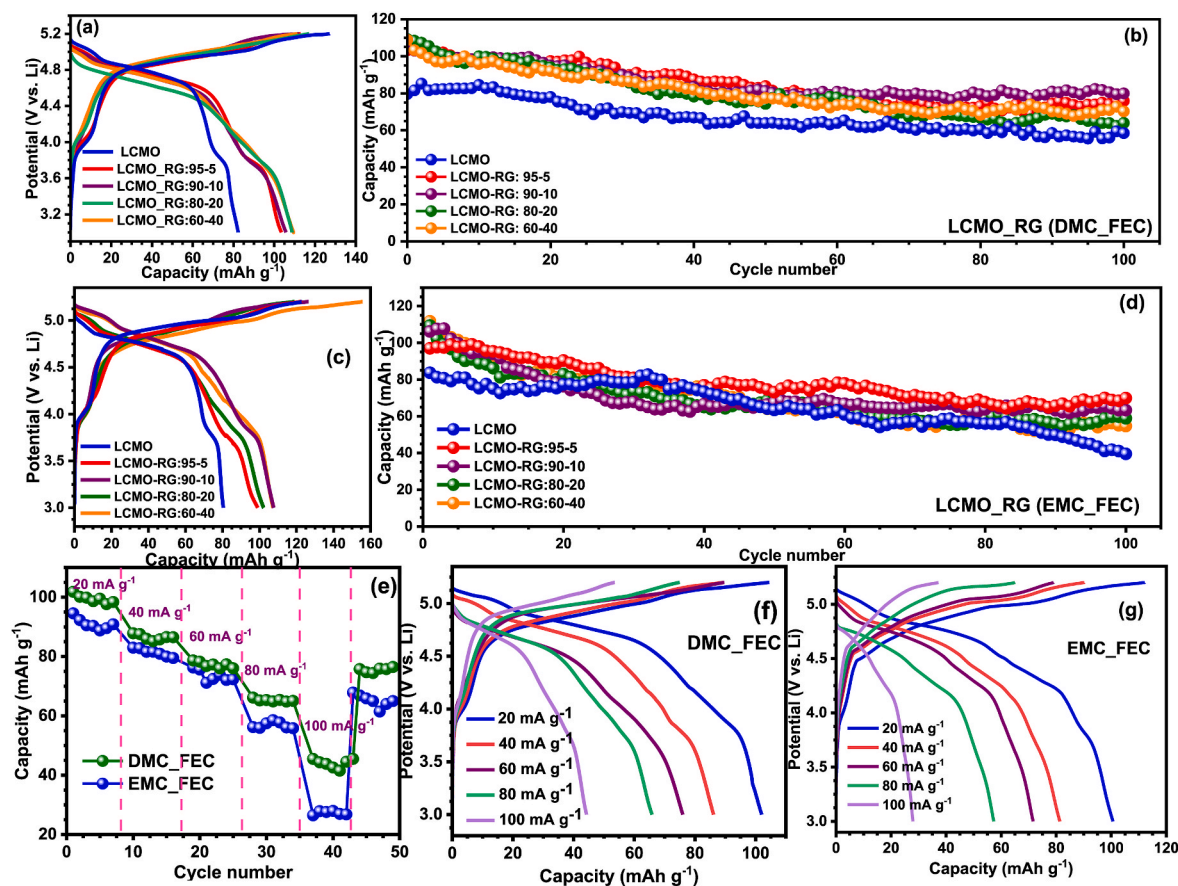


Fig. 4. Plot showing (a) charge-discharge curves and (b) capacity vs. cycle number plot of LCMO_RG cycled in DMC_FEC electrolyte, (c) charge-discharge curves and (d) capacity vs. cycle number plot of LCMO_RG cycled in EMC_FEC electrolyte, (e) rate performance study of LCMO_RG: 60–40 in DMC_FEC and EMC_FEC, and (f, g) charge-discharge curves of LCMO_RG in DMC_FEC and EMC_FEC at different cycle numbers within the potential window of 3–5.2 V vs. Li.

corresponding to the $\text{Mn}^{4+}/\text{Mn}^{3+}$ and $\text{Co}^{3+}/\text{Co}^{2+}$ redox couples. The LCMO_RG cycled in DMC_FEC exhibits low polarization, while that cycled in EMC_FEC shows polarization with additional stray peaks corresponding to the electrolyte decomposition. This can be attributed to the poor oxidation stability of EMC, which causes electrolyte decomposition in EMC_FEC, while DMC's relatively higher oxidation stability does not cause electrolyte degradation in DMC_FEC. The aforementioned facts can be observed from the LSV result, wherein DMC_FEC exhibits oxidation stability to a potential of ~ 5.0 V vs. Li, while the EMC_FEC is stable only to a potential of ~ 4.5 V vs. Li.

The kinetics of the electrochemical reactions associated with LCMO_RG have been investigated using the electrochemical impedance spectroscopy (EIS) analysis. A Nyquist plot (Fig. S7b) consists of a solution resistance (R_s) and a charge-transfer resistance (R_{CT}) at the high-frequency region, while the low-frequency region consists of a rising Warburg (Z_w) curve illustrating the mass-transfer region. The Nyquist plot of the LCMO_RG composites depicts a trend in which a decrement in the magnitude of R_{CT} can be observed as the RG content is increased from 5 to 40 wt%. This trend in the magnitude of R_{CT} can be attributed to the enhancement in the Li-ion transfer kinetics with an increase in the amount of the RG content. In addition, improving the stability of the SEI layer by RG mitigates the irreversible capacity loss due to electrolyte decomposition, further improving the Li-ion mobility, hence the kinetics of the electrochemical reaction. *In-situ* impedance (Fig. S8) analysis has been carried out to understand the nature of the SEI layer and its evolution as cycling progresses. The *in-situ* impedance plot depicts an increase in the magnitude of R_{CT} in the initial cycle due to electrolyte decomposition forming an SEI layer. However, a drastic decrease in the magnitude of R_{CT} can be observed as the cycling progresses to the 10th cycle due to the stabilization of the formed SEI layer by the RG component. Furthermore, the magnitude of R_{CT} remains stable as the cycling proceeds to the 50th and 100th cycle. This trend in the magnitude of R_{CT} can be attributed to the formation and stabilization of the SEI layer. In the first cycle, the decomposition of the electrolytes upon charging to a potential of 5.2 V vs. Li will lead to their decomposition, forming an SEI layer and increasing the magnitude of R_{CT} . As the cycling progresses to the 10th cycle, the magnitude of R_{CT} drastically decreases due to improved stability of the SEI layer by the FEC component in the electrolyte, showing no more electrolyte decomposition. In addition, a decrement in the magnitude of R_{CT} can be observed in the 50th and then in the 100th cycle, showing the long-term stability of the as-formed SEI layer. In other words, it depicts the enhanced stability of the optimized electrolyte.

The determination of the apparent diffusion coefficient (D_{Li^+}) was carried out using the Nyquist plot. From the Nyquist plot, the slope of the Z vs. $\omega^{-1/2}$ plot (Fig. S9) has been used for the evaluation of the D_{Li^+} , using the equation [16,19],

$$D_{Li^+} = R^2 T^2 / 2 A^2 n^4 F^4 \sigma_w^2 C^2 \quad (\text{iii})$$

Where R refers to the universal gas constant, T refers to the temperature, A is the cross-sectional area of the electrode, n is the number of Li-ions involved in the charge-discharge, F is the Faraday constant ($96,500 \text{ C mol}^{-1}$), σ_w is the slope of the Z vs. $\omega^{-1/2}$, and C is the concentration of the electrolyte. The apparent diffusion coefficient exhibits a magnitude in the order of $\sim 10^{-14} \text{ m}^2 \text{ s}^{-1}$. The as-determined magnitudes of diffusion coefficients (Table T1) for LCMO_RG exhibit a trend in which the D_{Li^+} shows a direct proportionality with the amount of RG present, where D_{Li^+} shows an increment in its magnitude as the amount of RG is increased from 5 to 20 wt%, while a slight decrement in its magnitude can be observed as the amount of RG is increased to 60 wt%. This trend in the D_{Li^+} can be explained by the high conductivity of RG, wherein the addition of 5–20 wt% of RG with LCMO exhibits an increase in the Li-ion diffusion due to the additional channels provided by RG on the surface of LCMO. On the other hand, a slight decrement in the D_{Li^+} for 60 wt% is due to the high concentration of RG content on the surface of LCMO, causing

hindrance to the Li-ion diffusion.

The capacitive effect on the charge storage mechanism occurring in LCMO_RG has been evaluated from the CV performed at scan rates from 0.1 to 2 mV s^{-1} . From the power law equation, the peak current holds a direct proportionality with the scan rate, given by [32].

$$i = a \times v^b \quad (\text{iv})$$

$$\ln(i) = \ln(a) + b \ln(v) \quad (\text{v})$$

Where i is the peak current, v is the scan rate, a is the x-intercept, and b is the slope of the curve. The magnitude of b , determined from the $\log(i)$ vs. $\log(v)$ plot (Fig. S10), yields information on the nature of the charge storage mechanism. For $b = 0.5$, the mechanism is intercalation-controlled, while for $b = 1$, the mechanism is solely capacitive-controlled. However, the mechanism is both intercalation and capacitive-assisted if the magnitude of b lies within the range of 0.5–1. In LCMO_RG, the b -value has been determined for the oxidation peak at 5.1 V vs. Li corresponding to PF_6^- intercalation and for the reduction peak at 4.8 V vs. Li, for the RG composition ranging from 5 to 40 wt%. The magnitude of b for the LCMO_RG at a potential of 5.1 V vs. Li falls well within the range of 0.5–1, showing that the mechanism is both capacitive and intercalation-assisted. In addition, a rise in the magnitude of b from 0.53 to 0.72 can be observed as the RG content is increased from 5 to 40 wt%. This indicates an increase in the capacitive contribution, specifically an enhancement in the pseudo-capacitive reaction. Hence, intercalation and a pseudocapacitive charge storage mechanism indicate the hybrid nature of the LCMO_RG.

An *in-situ* XRD analysis (Fig. S11) has been conducted to understand the mechanism underlying dual-ion de-/intercalation in LCMO_RG. For the study, an *in-situ* cell was fabricated with LCMO_RG: 80–20 against Li as the counter electrode, and the cell was subjected to electrochemical testing within the potential range of 3–5.2 V vs. Li. The peak shift and generation of new peaks have been analyzed for the reflections corresponding to RG for (002) ($\sim 25.5^\circ$) and LCMO for (333) ($\sim 59.57^\circ$) crystal planes [27]. In the case of LCMO, the (333) diffraction peak does not undergo any peak shift within 3.3–4.5 V vs. Li. However, a prominent peak shift can be observed (~ 0.1 – 0.5°) as the LCMO_RG is charged beyond 4.7 V vs. Li due to the oxidation of Co^{3+} to Co^{4+} . Also, the underlying mechanism for the charge-discharge in LCMO is a solid solution mechanism where a single phase remains active during the entire voltage range. Accordingly, the (002) peaks of the RG component remain dormant at low potentials (3–4.4 V vs. Li). However, as the charging progresses within a potential range of 4.5–4.7 V (vs. Li), a slight peak shift can be observed, showing the initiation of PF_6^- intercalation into RG, forming a Stage-3 graphite intercalation compound, C_{72}PF_6 . Now, as the charging progresses to a potential range of 4.8–5 V vs. Li, the PF_6^- intercalation becomes more pronounced, leading to the formation of Stage-2 graphite intercalation compounds (GICs), C_{48}PF_6 , leading to a prominent peak shift. However, as the charging progresses beyond 5 V vs. Li, the complete PF_6^- intercalation occurs, leading to the formation of Stage-1 GICs, C_{24}PF_6 , where the (002) diffraction peaks become more intense and also a significant peak shift of $\sim 0.8^\circ$ can be observed. Hence, unlike LNMO_Graphite, where partial anion intercalation occurs due to a restricted upper cut-off potential (~ 4.9 V vs. Li), the LCMO_RG exhibits complete anion intercalation, forming the Stage-1 GIC [27]. Similarly, the plateaus for the anion intercalation into graphite are overshadowed by the polarization of the Li-insertion/extraction process in LCMO. Therefore, the novelty of this simultaneous process lies in the fact that complete utilization of the potential window of RG has been achieved during the GCD cycling of LCMO_RG, which eventually leads to enhancement in the capacity and redox activity at high operating potentials. A detailed (de-) intercalation mechanism for the PF_6^- and Li-ion into LCMO_RG is given in Scheme 1.

The post-analysis of the LCMO_RG electrodes has been performed using XRD and XPS techniques to investigate the occurrence of any

phase change or electrolyte decomposition during charge-discharge cycling. The XRD spectra (Fig. S12a) of cycled LCMO_RG electrodes exhibit characteristic diffraction peaks corresponding to (111), (002), (311), (444), and (440) crystal planes of the pristine LCMO_RG samples. Additionally, no peak shift or peak generation can be observed in the cycled LCMO_RG electrodes, which is consistent with the fact that no phase change or structural deformation has occurred in the LCMO_RG as the cycling progresses. However, the poor intensity of the (002) peaks among the LCMO_RG electrodes cycled in EMC-FEC is due to the surface disruption of the coated RG on the surface of LCMO_RG, due to poor stability of the electrolyte, forming an unstable SEI layer. On the other hand, the LCMO_RG cycled in DMC-FEC shows comparatively higher intensity (002) diffraction peaks than EMC-FEC due to the formation of a stable SEI layer, preventing the disruption of the surface-coated RG. The XPS analysis (Fig. S12b–e) of the cycled LCMO_RG electrodes shows the presence of C, O, Mn, and Co on the surface of the material. The deconvolution of the C 1s core level exhibits peaks corresponding to C—C (284.4 eV) and C=C (285.3 eV), which shows the RG component in the compound, while the O 1s core level on deconvolution yields peaks corresponding to the C=O (531.5 eV), and C—O (533.4 eV). The C 1s spectra exhibit C—C and C=C peaks of similar intensity to that of pristine LCMO_RG, which shows that the RG component had not undergone any structural deformation even after prolonged cycling. However, the intensity of the C—O and C=O peaks in the cycled LCMO_RG electrode shows a slight deterioration compared to pristine LCMO_RG. The transition metal peaks of Mn (Mn 2p_{1/2} and Mn 2p_{3/2}) and Co (Co 2p_{1/2} and Co 2p_{3/2}) in the cycled LCMO_RG electrodes exhibit oxidation states of +4 and +3, which is in agreement with the absence of any phase change or structural deformation. In addition, the intense peaks of Co and Mn in the cycled LCMO_RG electrode are in agreement with the absence of any transition metal dissolution. Therefore, the XRD and XPS post-analysis studies have further confirmed the absence of any phase change or structural deformation with LCMO_RG upon prolonged electrochemical cycling.

The FE-SEM analysis of the cycled and uncycled LCMO_RG electrodes (Fig. S13) was carried out to understand any degradation of the electrode materials. The uncycled LCMO_RG electrodes show spherical-shaped LCMO particles covered with flaky RG particles. However, the surface of cycled electrodes is distorted due to electrolyte decomposition and parasitic side reactions. However, the spherical shape of the LCMO particles is preserved due to the RG coating on their surface. Further, the FE-SEM image of the cycled LCMO_RG electrodes shows good interaction between the LCMO and RG.

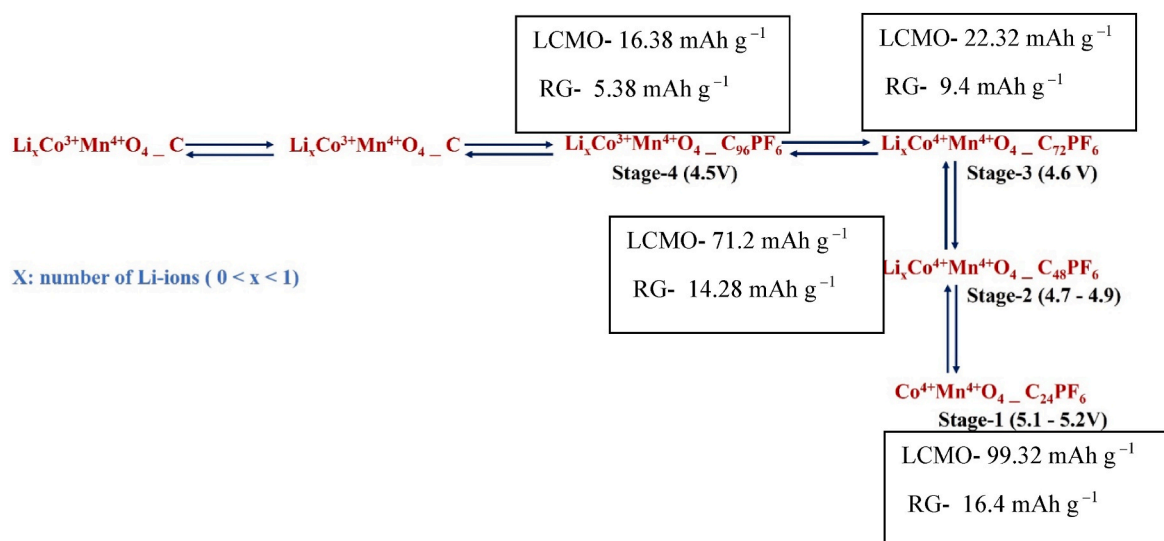
3.5. Full- and anode-less cell electrochemical studies

The full cell fabrication has been carried out with LCMO_RG against Li₄Ti₅O₁₂ (LTO) as the counter electrode using electrolyte combinations of DMC_FEC and EMC_FEC within a potential window of 1.5–3.7 V. The GCD profile of LCMO_RG\LTO cycled in DMC_FEC (Fig. 5c and d) exhibits an enhancement in the electrochemical performance with an initial discharge capacity of 99 mA h g^{−1}, capacity retention of 80% and coulombic efficiency of 98% after 100 cycles. In contrast, LCMO_RG\LTO cycled in EMC_FEC (Fig. 5a and b) exhibits poor capacity retention of 74% after 100 cycles, which is low compared to the LCMO_RG\LTO cycled in DMC_FEC. The temperature study of the LCMO_RG\LTO cell (Fig. 5g) has been conducted within the range −10 to 70 °C to depict its practical applicability at various climatic conditions. At low temperatures of 0 and −10 °C, the LCMO_RG\LTO cell exhibits poor electrochemical performance due to the freezing up of electrolytes, leading to poor mobility of anion and cation, hence degrading the electrochemical performance. In contrast, at high temperatures of 50 and 70 °C, there is an enhancement in the electrochemical performance of LCMO_RG\LTO due to the fast ion mobility by thermal agitation.

The anode-less cell study (Fig. 5e and f) has been carried out by pairing the optimized LCMO_RG against Cu as a counter electrode, LCMO_RG\Cu, using the DMC_FEC electrolyte and cycled within the potential window of 2.9–5.1 V. The GCD profile of LCMO_RG\Cu exhibits an excellent initial discharge capacity of 79 mA h g^{−1} with capacity retention and coulombic efficiency of 74 and 97% after 50 cycles. This enhancement in the electrochemical performance in the LCMO_RG\Cu is due to the excellent stability of the electrolyte at high operating potential, thereby mitigating its decomposition. Although, the previous reports in anode-less configuration have been focused on the stabilization of <5 V class cathodes, particularly in LiNi_{0.5}Mn_{1.5}O₄ using a ternary salt-solvent electrolyte, this has been the first report among the >5 V vs. Li class cathodes, particularly hybrid cathodes, by incorporating the dual-ion de-/intercalation concept [33].

4. Conclusion

Here, we successfully demonstrate the dual-ion de-/intercalation of Li⁺ and PF₆[−] into the LCMO_RG hybrid cathode [39,40]. The GCD study depicted the superior electrochemical performance of LCMO_RG compared to the pristine LCMO. From the preliminary electrochemical study, the suitable composite and electrolyte have been optimized to be LCMO_RG: 80–20 and DMC_FEC, respectively. The impedance analysis



Scheme 1. Detailed reaction mechanism of anion intercalation into LCMO_RG [34].

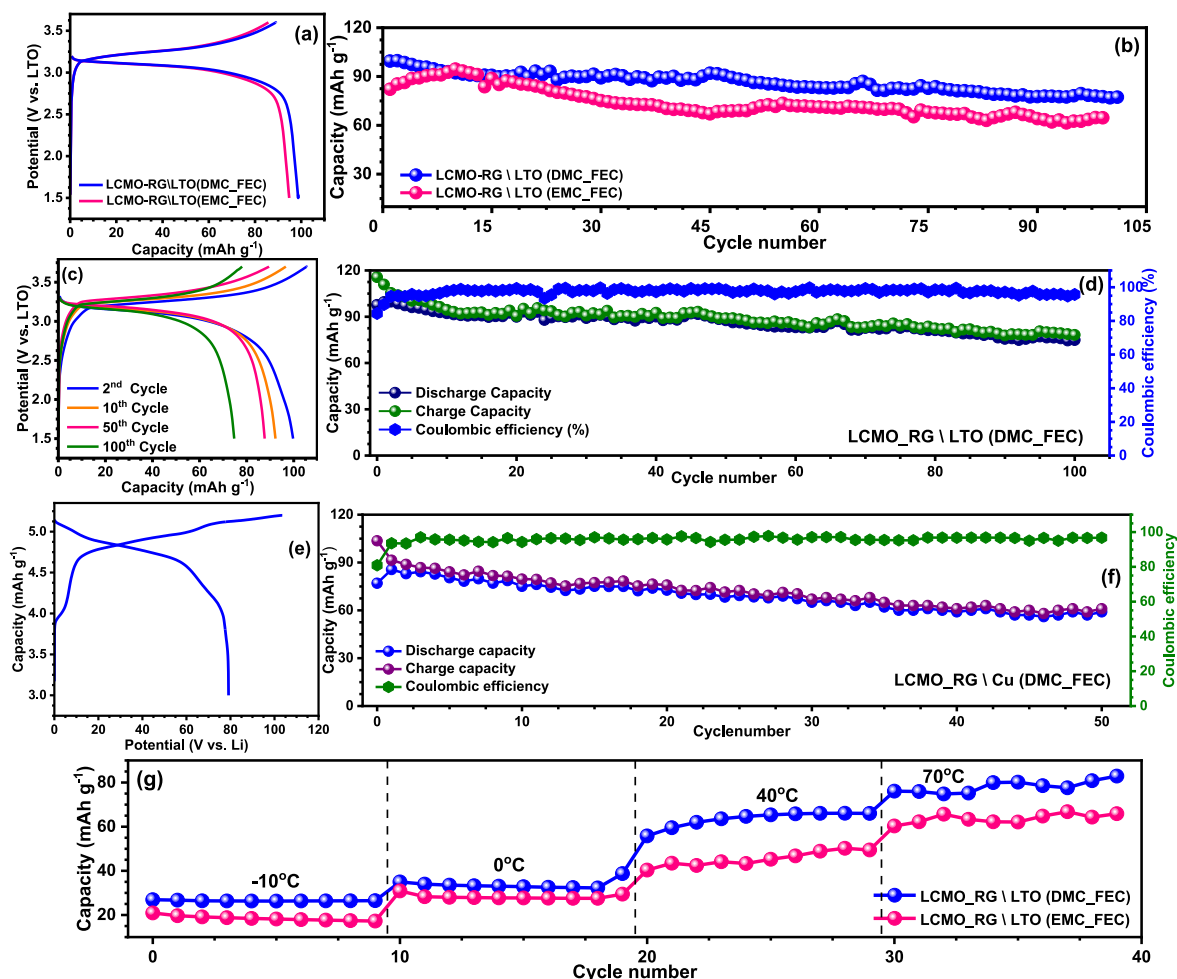


Fig. 5. Plot showing the (a) charge-discharge curves, (b) capacity vs. cycle number plot for LCMO_RG/LTO cycled in DMC_FEC and EMC_FEC, (c) charge-discharge curves at 2nd, 10th, 50th, and 100th cycle, (d) charge, discharge, and coulombic efficiency vs. cycle number plot for LCMO_RG/LTO cycled in DMC_FEC, (e, f) charge-discharge curve and capacity vs. cycle number plot for anode-less LCMO_RG/Cu configuration, and (g) temperature study of LCMO_RG/LTO at temperature ranging from −10 to 70 °C within the potential window of 1.4–3.7 V.

has shown a decrease in the magnitude of R_{CT} as the RG content in LCMO_RG is increased from 5 to 40 wt%. Further, the *in-situ* impedance analysis illustrates the role of RG in stabilizing the SEI layer formed due to electrolyte decomposition. The post-analysis of the LCMO_RG electrodes carried out using XRD, XPS, and NMR analysis does not depict any sign of structural distortion or electrolyte decomposition during electrochemical cycling. The full-cell electrochemical studies of the LCMO_RG/LTO exhibited an enhancement in the electrochemical performance in the case of DMC_FEC compared to the EMC_FEC. In addition, the anode-less cell configuration, LCMO_RG/Cu, depicted excellent capacity retention and coulombic efficiency compared to the previous reports. From a future point of view, the study of hybrid materials can be extended toward coupling the high-voltage cathodes with materials such as MXenes, graphenes, etc. Also, the usage of solid electrolytes, particularly gel-polymer-based (GPE) electrolytes, can mitigate the issue of electrolyte decomposition and poor cycle stability among hybrid high-voltage cathodes to a certain extent.

CCRediT authorship contribution statement

Sreekumar Sreedeeep: Writing – review & editing, Writing – original draft, Investigation, Formal analysis, Data curation, Conceptualization. **Karayi Mangat Athira:** Writing – original draft, Validation, Investigation, Formal analysis, Data curation. **Yun-Sung Lee:** Writing – review & editing, Validation, Funding acquisition, Data curation. **Vanchiappan**

Aravindan: Writing – review & editing, Writing – original draft, Validation, Supervision, Project administration, Funding acquisition, Formal analysis, Data curation, Conceptualization.

Declaration of competing interest

The authors declare that they have no known competing financial interests or personal relationships that could have appeared to influence the work reported in this paper.

Acknowledgement

SS acknowledges the Council of Scientific and Industrial Research (CSIR), Govt. of India for the fellowship. YSL acknowledges the financial support from the National Research Foundation of Korea (NRF) grant funded by the Korean government (Ministry of Science, ICT & Future Planning) (No. RS-2023-00208361). VA acknowledges financial support from the Anusandhan National Research Foundation (ANRF), Govt. of India, through Swarnajayanti Fellowship (SB/SJF/2020–21/12).

Appendix A. Supplementary data

Supplementary data to this article can be found online at <https://doi.org/10.1016/j.jpowsour.2025.238366>.

Data availability

Data will be made available on request.

References

- [1] S. Sreekumar, S. Natarajan, V. Aravindan, Recent advancements in LiCoPO₄ cathodes using electrolyte additives, *Curr. Opin. Electrochem.* 31 (2021) 100868, <https://doi.org/10.1016/j.coelec.2021.100868>.
- [2] V. Etacheri, R. Marom, R. Elazari, G. Salitra, D. Aurbach, Challenges in the development of advanced Li-Ion batteries: a review, *Energy Environ. Sci.* 4 (9) (2011) 3243–3262, <https://doi.org/10.1039/c1ee01598b>.
- [3] A. Manthiram, An outlook on lithium ion battery technology, *ACS Cent. Sci.* 3 (10) (2017) 1063–1069, <https://doi.org/10.1021/acscentsci.7b00288>.
- [4] X. Yu, W.A. Yu, A. Manthiram, Advances and prospects of high-voltage spinel cathodes for lithium-based batteries, *Small Methods* 5 (5) (2021) 2001196, <https://doi.org/10.1002/smt.202001196>.
- [5] S.S. Zhang, K. Xu, T.R. Jow, Study of the charging process of a LiCo₂O₄-based Li-Ion battery, *J. Power Sources* 160 (2) (2006) 1349–1354, <https://doi.org/10.1016/j.jpowsour.2006.02.087>.
- [6] Y. Lyu, X. Wu, K. Wang, Z. Feng, T. Cheng, Y. Liu, M. Wang, R. Chen, L. Xu, J. Zhou, Y. Lu, B. Guo, An overview on the advances of LiCo₂O₄ cathodes for lithium-ion batteries, *Adv. Energy Mater.* 11 (2) (2021) 2000982, <https://doi.org/10.1002/aenm.202000982>.
- [7] J.-N. Zhang, Q. Li, C. Ouyang, X. Yu, M. Ge, X. Huang, E. Hu, C. Ma, S. Li, R. Xiao, W. Yang, Y. Chu, Y. Liu, H. Yu, X.-Q. Yang, X. Huang, L. Chen, H. Li, Trace doping of multiple elements enables stable battery cycling of LiCo₂O₄ at 4.6 V, *Nat. Energy* 4 (7) (2019) 594–603, <https://doi.org/10.1038/s41560-019-0409-z>.
- [8] S. Oh, J. Lee, D. Byun, W. Cho, W. Cho, Effect of Al₂O₃ coating on electrochemical performance of LiCo₂O₄ as cathode materials for secondary lithium batteries, *J. Power Sources* 132 (2004) 249–255, <https://doi.org/10.1016/j.jpowsour.2004.01.049>.
- [9] J. Qian, L. Liu, J. Yang, S. Li, X. Wang, H.L. Zhuang, Y. Lu, Electrochemical surface passivation of LiCo₂O₄ particles at ultrahigh voltage and its applications in lithium-based batteries, *Nat. Commun.* 9 (1) (2018) 4918, <https://doi.org/10.1038/s41467-018-07296-6>.
- [10] S. Sreedeeep, Y.-S. Lee, V. Aravindan, Functional AlF₃ modification over 5.3 V spinel LiCoMnO₄ cathode for Li-Ion batteries, *Compos. B Eng.* (2024) 111365, <https://doi.org/10.1016/j.compositesb.2024.111365>.
- [11] S. Sreedeeep, Y.-S. Lee, V. Aravindan, Probing enhanced electrochemical performance of poly (3,4-Ethylenedioxy thiophene) encapsulated 5.3 V spinel LiCoMnO₄ cathode for Li-Ion batteries, *Adv. Sustain. Syst.* 7 (12) (2023) 2300267, <https://doi.org/10.1002/advsu.202300267>.
- [12] A. Windmüller, C.A. Bridges, C.L. Tsai, S. Lobe, C. Dellen, G.M. Veith, M. Finsterbusch, S. Uhlenbruck, O. Guillon, Impact of fluorination on phase stability, crystal chemistry, and capacity of LiCoMnO₄ high voltage spinels, *ACS Appl. Energy Mater.* 1 (2) (2018) 715–724, <https://doi.org/10.1021/acsaem.7b00186>.
- [13] S. Liu, H. He, D. Zhang, C. Chang, Cr-Doped LiCoMnO₄ cathode with high phase purity and promoted electrochemical performance, *Int. J. Energy Res.* 45 (11) (2021) 16538–16550, <https://doi.org/10.1002/er.6901>.
- [14] N. Reeves-McLaren, M. Hong, H. Alqurashi, L. Xue, J. Sharp, A.J. Rennie, R. Boston, The spinel LiCoMnO₄: 5 V cathode and conversion anode, *Energy Proc.* 151 (2018) 158–162, <https://doi.org/10.1016/j.egypro.2018.09.041>.
- [15] E. Zhecheva, R. Stoyanova, R. Alcántara, P. Lavela, J.L. Tirado, EPR studies of Li deintercalation from LiCoMnO₄ spinel-type electrode active material, *J. Power Sources* 159 (2) (2006) 1389–1394, <https://doi.org/10.1016/j.jpowsour.2005.11.088>.
- [16] S. Sreekumar, S. Praneetha, Y. Lee, V. Aravindan, Influence of lithium difluoro (Oxalato) borate additive on the performance of LiCoPO₄ - LiFePO₄ solid-solution by carbothermal reduction, *ChemElectroChem* 9 (2022) e202200815, <https://doi.org/10.1002/celec.202200815>.
- [17] S. Sreekumar, V. Aravindan, Fabrication of 4.7 V class “Rocking-Chair” type Li-Ion cells with carbon-coated LiCoPO₄ as cathode and Graphite anode, *Mater. Lett.* 291 (2021) 129609, <https://doi.org/10.1016/j.matlet.2021.129609>.
- [18] S. Sreedeeep, S. Natarajan, Y.S. Lee, V. Aravindan, Stabilizing the high voltage LiCoPO₄ cathode via Fe-Doping in the gram-scale synthesis, *Electrochim. Acta* 419 (2022), <https://doi.org/10.1016/j.electacta.2022.140367>.
- [19] S. Sreedeeep, S. Natarajan, Y.-S. Lee, V. Aravindan, Lithium Difluoro(Oxalate) Borate-Induced interphase for high-voltage LiFe_{0.15}Co_{0.85}PO₄/C cathode by solid-state synthesis, *Energy Technol.* 11 (1) (2023) 2200988, <https://doi.org/10.1002/ente.202200988>.
- [20] S.S. Nair, B.R. Isaac, S. Alwarappan, S. Sreedeeep, V.K. Pillai, Electroformation and room-temperature doping of graphene nanoribbons for energy storage applications, *ACS Appl. Nano Mater.* 7 (7) (2024) 7337–7344, <https://doi.org/10.1021/acsnm.4c00033>.
- [21] J. Holoubek, Z. Chen, P. Liu, Application-Based prospects for dual-ion batteries, *ChemSusChem* 16 (4) (2023) e202201245, <https://doi.org/10.1002/cssc.202201245>.
- [22] J. Hao, X. Li, X. Song, Z. Guo, Recent progress and perspectives on dual-ion batteries, *Energy* 1 (1) (2019) 100004, <https://doi.org/10.1016/j.enchem.2019.100004>.
- [23] X. Zhou, Q. Liu, C. Jiang, B. Ji, X.L. Ji, Y. Tang, H.M. Cheng, Strategies towards low-cost dual-ion batteries with high performance, *Angew. Chem., Int. Ed.* 59 (10) (2020) 3802–3832, <https://doi.org/10.1002/anie.201814294>.
- [24] L. Zhang, H. Wang, X. Zhang, Y. Tang, A review of emerging dual-ion batteries: fundamentals and recent advances, *Adv. Funct. Mater.* 31 (20) (2021) 2010958, <https://doi.org/10.1002/adfm.202010958>.
- [25] Z. Guo, Z. Xu, F. Xie, J. Feng, M. Titirici, Strategies for high energy density dual-ion batteries using carbon-based cathodes, *Adv. Energy Sustain. Res.* 2 (11) (2021), <https://doi.org/10.1002/aesr.202100074>.
- [26] Y.-B. Fang, W. Zheng, T. Hu, L. Li, W.-H. Yuan, High-performance dual-ion battery based on a layered tin disulfide anode, *ACS Omega* 7 (9) (2022) 7616–7624, <https://doi.org/10.1021/acsomega.1c06134>.
- [27] S. Künne, J.M. Hesper, T. Lein, K. Voigt, D. Mikhailova, A. Michaelis, M. Winter, T. Placke, C. Heubner, Hybrid high-voltage LiNi_{0.5}Mn_{1.5}O₄/Graphite cathodes enabling rechargeable batteries with simultaneous Anion- and cation storage, *Batteries Supercaps* 6 (9) (2023), <https://doi.org/10.1002/batt.202300284>.
- [28] K. Striebel, J. Shim, A. Sierra, H. Yang, X. Song, R. Kostecki, K. McCarthy, The development of low cost LiFePO₄-based high power Lithium-Ion batteries, *J. Power Sources* 146 (1) (2005) 33–38, <https://doi.org/10.1016/j.jpowsour.2005.03.119>.
- [29] F. Jiang, K. Qu, M. Wang, J. Chen, Y. Liu, H. Xu, Y. Huang, J. Li, P. Gao, J. Zheng, M. Chen, X. Li, Atomic Scale insight into the fundamental mechanism of Mn Doped LiFePO₄, *Sustain. Energy Fuels* 4 (6) (2020) 2741–2751, <https://doi.org/10.1039/D0SE00312C>.
- [30] K.J. Kreder, A. Manthiram, Vanadium-Substituted LiCoPO₄ core with a monolithic LiFePO₄ shell for high-voltage Lithium-Ion batteries, *ACS Energy Lett.* 2 (1) (2017) 64–69, <https://doi.org/10.1021/acsenenergylett.6b00496>.
- [31] M.L. Divya, S. Natarajan, Y.-S. Lee, V. Aravindan, Highly reversible Na-Intercalation into graphite recovered from spent Li-Ion batteries for high-energy Na-Ion capacitor, *ChemSusChem* 13 (21) (2020) 5654–5663, <https://doi.org/10.1002/cssc.202001355>.
- [32] A. Cymann-Sachajdak, M. Graczyk-Zajac, G. Trykowski, M. Wilamowska-Zawłocka, Understanding the capacitance of thin composite films based on conducting polymer and carbon nanostructures in aqueous electrolytes, *Electrochim. Acta* 383 (2021) 138356, <https://doi.org/10.1016/j.electacta.2021.138356>.
- [33] S. Pal, X. Lin, P. Apostol, C. Ungureanu, D. Tie, V.R. Bakuru, D. Rambabu, N. Campagnol, A. Kachmar, C. Poleunis, G. Barozzino-Consiglio, M. Buga, A. Vlad, Ternary salt-solvent electrolytes for 5 V-Class anode-less Li-Metal batteries, *ACS Energy Lett.* 9 (9) (2024) 4399–4407, <https://doi.org/10.1021/acsenenergylett.4c01435>.
- [34] Y. Matsuo, A. Inoo, J. Inamoto, Electrochemical intercalation of anions into graphite: fundamental aspects, material synthesis, and application to the cathode of dual-ion batteries, *Chem. Open* 13 (8) (2024) e202300244, <https://doi.org/10.1002/open.202300244>.
- [35] N. Wu, W. He, S. Shi, X. Yuan, J. Li, J. Cao, C. Yuan, X. Liu, Bamboo fiber-derived carbon support for the immobilization of Pt nanoparticles to enhance hydrogen evolution reaction, *J. Colloid Interface Sci.* 684 (P1) (2025) 658–667, <https://doi.org/10.1016/j.jcis.2025.01.071>.
- [36] N. Wu, Z. Zhao, Y. Zhang, R. Hua, J. Li, G. Liu, D. Guo, J. Zhao, A. Cao, G. Sun, H. Hou, X. Liu, Revealing the fast reaction kinetics and interfacial behaviors of CuFe₂ hollow nanorods for durable and high-rate sodium storage, *J. Colloid Interface Sci.* 679 (PB) (2025) 990–1000, <https://doi.org/10.1016/j.jcis.2024.10.175>.
- [37] J. Guo, Y. Xu, M. Exner, X. Huang, Y. Li, Y. Liu, H. Wang, J. Kowal, Q. Zhang, P. K. Kristensen, D. Wang, K. Pedersen, L. Gurevich, D.-I. Stroe, P. Adelhelm, Unravelling the mechanism of pulse current charging for enhancing the stability of commercial LiNi_{0.5}Mn_{0.3}Co_{0.2}O₂/Graphite Lithium-Ion batteries, *Adv. Energy Mater.* 14 (22) (2024) 2400190, <https://doi.org/10.1002/aenm.202400190>.
- [38] S. Sreedeeep, Y.S. Lee, V. Aravindan, In-situ transformation of liquid electrolyte into the solid polymer electrolyte: influence of TMSP with layered LiNi_{0.82}Mn_{0.12}Al_{0.06}O₂ cathode, *J. Mater. Chem.* 13 (2025) 13262–13275, <https://doi.org/10.1039/d4ta08731c>.
- [39] S. Sreedeeep, K.M. Athira, Y.-S. Lee, V. Aravindan, Crucial role of solvent and additive during the transformation of liquid to solid polymer electrolyte for stabilizing 4.8 V class LiCo_{0.9}Fe_{0.1}PO₄ cathode in anode and anodeless assemblies, *Small* 21 (2025) 2503310, <https://doi.org/10.1002/sml.202503310>.
- [40] S. Sreedeeep, Y.-S. Lee, V. Aravindan, Tailoring the salt concentration in a gel-solid polymer electrolyte to stabilize high-voltage LiCoMnO₄ cathode, *Small* 21 (2025) 2503594, <https://doi.org/10.1002/sml.202503594>.